

The structure of the compact planetary nebulae Cn 3-1 and M 3-27 and their extended haloes

Luis F. Miranda,^{1,2★} Roberto Vázquez,^{2★} José M. Torrelles,^{2★} Carlos Eiroa^{3★}
and J. Alberto López^{4★}

¹*Departamento de Astrofísica, Facultad de Ciencias Físicas, Universidad Complutense de Madrid, E-28040 Madrid, Spain*

²*Instituto de Astrofísica de Andalucía, CSIC, Ap. Correos 3004, C/ Sancho Panza s/n, E-18080 Granada, Spain*

³*Departamento de Física Teórica CXI, Facultad de Ciencias, Universidad Autónoma de Madrid, Cantoblanco, E-28049 Madrid, Spain*

⁴*Instituto de Astronomía, UNAM, Apartado Postal 877, Ensenada B.C., 22830 México*

Accepted 1997 March 12. Received 1997 March 6; in original form 1996 December 28

ABSTRACT

We present long-slit optical spectroscopy and VLA-B radio continuum ($\lambda = 3.6$ cm) observations of the compact planetary nebulae Cn 3-1 and M 3-27. The data allow us to distinguish different regions in both objects, to study their kinematical and emission properties, and to deduce different physical parameters in both nebulae. The radio and optical data show that the ionized shell of Cn 3-1 is an ellipsoid containing a bright, ring-like equatorial zone (size $\simeq 2.6$ arcsec, expansion velocity $\simeq 14$ km s⁻¹). Two bright, point-symmetric arcs have been detected in the core of Cn 3-1, extending from the equator towards the polar regions of the ellipsoid. The arcs seem to be filamentary structures located on the ellipsoid. The origin of the arcs could be related to some sort of collimated bipolar ejections along a rotating axis. Relatively high mean [N II]/H $\alpha \simeq 0.83$ and [S II]/H $\alpha \simeq 0.056$ line intensity ratios are found in Cn 3-1. Maximum values of [S II]/H α of $\simeq 0.083$ are found in the arcs. The estimated kinematical age and ionized mass of Cn 3-1 are $\simeq 1300$ yr and $\simeq 4 \times 10^{-2} M_{\odot}$, respectively. M 3-27 is unresolved at 3.6 cm (size ≤ 0.6 arcsec). The detected [N II] and [S II] emission lines arise in a compact (size ≤ 1.4 arcsec), probably non-spherical region, which is identified with the ionized shell of M 3-27. The H α emission from M 3-27 is dominated by strong stellar emission and exhibits a type III P Cygni profile with very extended wings ($\simeq 3000$ km s⁻¹). A kinematical age of ≤ 530 yr and an ionized mass of $\simeq 3 \times 10^{-4} M_{\odot}$ are estimated for M 3-27. Extended haloes (size $\simeq 36$ arcsec in Cn 3-1, $\simeq 24$ arcsec in M 3-27) have been spectroscopically detected in both objects through their [N II] and/or H α emissions. An analysis of the kinematical and emission properties of the haloes strongly suggests that they are reflection nebulosities and contain large amounts of neutral material, and that the distribution of neutral material in them is largely isotropic.

Key words: ISM: kinematics and dynamics – planetary nebulae: individual: Cn 3-1 – planetary nebulae: individual: M 3-27 – radio continuum: ISM.

1 INTRODUCTION

In the last few years, as a consequence of significant improvements in the sensitivity and angular resolution of the observations, many new morphological features and kinematical components have been observed in planetary

nebulae (PNe), which are substantially changing our knowledge of these objects. In addition to the circular, elliptical, or bipolar morphologies previously identified, irregular morphologies and complex multishell systems are also found in a noticeable fraction of PNe (Balick 1987; Schwarz, Corradi & Melnick 1992). Small-scale structures, characterized by peculiar physical conditions, abundances and/or kinematics, are observed in many PNe (e.g. Balick et al. 1994; Corradi et al. 1996). Among these structures, highly collimated high-velocity knots and jet-like features are the

★E-mail: lfm@iaa.es (LFM); vazquez@iaa.es (RV);
torrelles@iaa.es (JMT); carlos@xiada.ft.uam.es (CE);
jal@bufadora.astrosen.unam.mx (JAL)

most outstanding (Giesekeing, Becker & Solf 1985; Miranda & Solf 1992; López, Meaburn & Palmer 1993; Solf 1994; Miranda 1995). The available theoretical models can explain the simplest morphologies, but are still unable to account for the rich and complex structural detail observed in most PNe.

Although the mass-ejection processes involved in the formation of PNe are still poorly known, the observations suggest that a large fraction of the observed structures result from or are related to mass ejections which occur in a relatively short time interval between the end of the AGB phase and the first stages of PN evolution. These ejections will determine many of the properties observed in evolved PNe. Observations of AGB stars, protoPNe and very young PNe are therefore necessary for a better understanding of how PNe are formed. Nowadays, the observational improvements mentioned above allow us a more detailed study of all these objects at different wavelength ranges (e.g. Miranda, Torrelles & Eiroa 1995; Hora & Latter 1996; Luhman & Rieke 1996). In particular, long-slit optical spectroscopy at high spectral and spatial resolution has proved to be one of the more powerful methods to identify the components present in a PN, to deduce their kinematical and emission properties, and to obtain estimates for the time when they were formed (e.g. Miranda 1995). Moreover, long-slit spectra complemented with radio continuum observations at high spatial resolution permit a very detailed picture of very young PNe to be obtained (Miranda, Torrelles & Eiroa 1996). However, the number of objects observed combining these techniques is still small. The variety of morphologies, structures and kinematics observed in PNe indicates that different mass-ejection processes may be forming different kinds of PNe. Hence it is interesting to increase the number of well-studied young PNe.

Cn 3-1 and M 3-27 are two young, compact PNe. Cn 3-1 is a low-excitation PN, which has an elliptical morphology of ≈ 8 arcsec in diameter (Schwartz et al. 1992). Very low expansion velocities of ≈ 4 and ≤ 10 km s $^{-1}$ have been obtained from the [O III] emission lines by Gussie & Taylor (1990) and Sabbadin, Bianchini & Hamzaoglu (1983), respectively. An electron density N_e of $\approx 4 \times 10^3$ cm $^{-3}$ and an electron temperature T_e of $\approx 10^4$ K have been deduced (Aller & Czyzak 1983; Kingsburgh & English 1992). Gurzadyan, Egikyan & Terzian (1991) reported the detection of Mg I absorption lines, which they attribute to a neutral envelope around the nebula. Most values for the distance to Cn 3-1 are concentrated between 2 and 3 kpc (Acker et al. 1992). We will adopt here an averaged value of 2.7 kpc. M 3-27 is stellar-like on direct H α and [O III] images (Schwartz et al. 1992). It is a high-excitation PN with strong [O III] emission (Feibelman 1985). The object presents a relatively high T_e of 15×10^3 K (Ahren 1978), whereas N_e has estimates in a wide range of values, from $N_e \approx 7.7 \times 10^5$ cm $^{-3}$ ([O III]) to $\approx 3.7 \times 10^3$ and 4.4×10^4 cm $^{-3}$ ([O II]) (Feibelman 1985, and references therein). Sabbadin (1984) obtained an expansion velocity of ≈ 13 km s $^{-1}$ from the [O III] emission lines. Photometry of lines and continuum has been made by Adams (1975), who estimated an effective temperature for the central star $\leq 55\,000$ K and reported self-absorbed H α arising in a compact region. The distance to M 3-27 is estimated to be ≈ 3 kpc (Cahn, Kaler & Stan-ghellini 1992).

We have obtained optical long-slit spectra and Very Large Array (VLA) radio continuum observations at 3.6 cm of Cn 3-1 and M 3-27, with the aim of studying their geometrical and kinematical properties. The results are presented in this work.

2 OBSERVATIONS

2.1 Optical spectroscopy

Long-slit spectra of Cn 3-1 and M 3-27 were obtained on 1993 July 12, 13 and 14 with the coude spectrograph of the 2.2-m telescope at Calar Alto Observatory.¹ The *f*/3 camera of the spectrograph was used. The detector was a TEK 24- μ m CCD with 1024×1024 pixel. The spectral range $\lambda\lambda 6540\text{--}6751$ Å was observed at a dispersion of 8.75 Å mm $^{-1}$. The slit was centred on the objects, and set at different position angles (PAs). In the case of Cn 3-1, four spectra at PAs 0°, 45°, 90° and 135° were obtained, whereas for M 3-27 two spectra at PAs 0° and 90° were taken. Exposure time was 1200 s for each spectrum. A Th-Ar lamp was used for wavelength calibration. The absolute error in radial velocities and velocity widths is estimated to be $\approx 3\text{--}5$ km s $^{-1}$; internal accuracy is much better (≤ 0.5 km s $^{-1}$). The achieved spectral resolution is ≈ 19 km s $^{-1}$. The spatial resolution (FWHM), mainly determined by the seeing, is ≈ 1.4 arcsec in M 3-27 and ≈ 2.0 arcsec in Cn 3-1. No flux calibration was carried out. The spectra were reduced using standard procedures for long-slit spectroscopy in the IRAF package.

2.2 Radio continuum

Continuum observations at $\lambda = 3.6$ cm toward Cn 3-1 and M 3-27 were made with the VLA of the National Radio Astronomy Observatory (NRAO)² during 1996 January 8 in the B-configuration. A bandwidth of 100 MHz and two circular polarizations were used. The absolute flux calibrator was 3C 286 (adopted flux density 5.27 Jy at 3.6 cm), while 1749 + 096 was used as phase calibrator (observed flux density 3.45 Jy at 3.6 cm). Phase centres were set at $[\alpha(1950), \delta(1950)] = [18^h 15^m 10^s.7, 10^\circ 08' 02'']$ (Cn 3-1 field) and $[18^h 25^m 31^s.6, 14^\circ 27' 11'']$ (M 3-27 field). The on-target integration time was 40 min in each case. The data were calibrated and processed using standard procedures of the Astronomical Image Processing System (AIPS) package of the NRAO. Cleaned natural-weight maps were obtained for Cn 3-1 (synthesized beam $\approx 0.88 \times 0.75$ arcsec 2 , PA = -23°) and M 3-27 (synthesized beam $\approx 0.81 \times 0.73$ arcsec 2 , PA = -18°). The noise level of the maps (≈ 30 μ Jy) is consistent with thermal noise. Extended continuum emission was detected toward Cn 3-1, while the emission was compact toward M 3-27, even using uniform-weight of the (*u, v*) data (synthesized beam ≈ 0.6 arcsec). Physical parameters of the radio continuum sources are given in Table 1.

¹The Calar Alto Observatory is operated by the Max-Planck-Institut für Astronomie (Heidelberg) and the Spanish Comisión Nacional de Astronomía.

²The NRAO is operated by Associated Universities Inc., under cooperative agreement with the National Science Foundation.

Table 1. VLA 3.6-cm radio continuum data.

Source	Position		Size (")	Flux (mJy)	N_e (10^3 cm^{-3})	EM (10^6 pc cm^{-6})	M(HII) (M_\odot)
	$\alpha(1950)$	$\delta(1950)$					
Cn 3-1	18 ^h 15 ^m 12 ^s .22	10°07'51".8	6×5	63	4	1	4×10^{-2}
M 3-27	18 ^h 25 ^m 31 ^s .60	14°27'09".8	≤ 0.6	0.9	9	1	3×10^{-4}

3 Cn 3-1

3.1 Results

A map of the radio continuum emission at 3.6 cm is shown in Fig. 1. The nebula appears as an ellipse with an angular size $\simeq 6 \times 5 \text{ arcsec}^2$ at the 3σ level and the major axis oriented at PA $\simeq 72^\circ$. Along the minor axis of the ellipse (PA $\simeq -18^\circ$) two maxima separated by $\simeq 2.6 \text{ arcsec}$ are observed. An emission arc extends from each of the maxima towards the polar regions of the ellipse. The arcs exhibit a remarkable point-symmetry with respect to the centre of the nebula (central position given in Table 1). Although the arcs closely follow the curvature of the ellipse, they do not connect the two maxima with each other. A maximum angular separation between the arcs of $\simeq 3.8 \text{ arcsec}$ is observed near the major nebular axis. The ‘radial thickness’ of the arcs, measured along the radial direction from the nebular centre (Table 1), is not resolved by the beam (radial thickness $\leq 0.75 \text{ arcsec}$). The total flux measured at 3.6 cm is 63 mJy. Assuming $T_e \simeq 10^4 \text{ K}$ (Aller & Czyzak 1983) and optically thin emission, and following Mezger & Henderson (1967), we estimate a mean $N_e \simeq 4 \times 10^3 \text{ cm}^{-3}$, emission measure $\text{EM} \simeq 10^6 \text{ pc cm}^{-6}$, and mass of ionized gas $M(\text{H II}) \simeq 0.04 M_\odot$ in a region of 6-arcsec size.

In our spectra H α , [N II] 6548, 6583, C II 6578, [S II] 6716, 6731 and He I 6678 emission lines are detected. We deduce a systemic velocity $V(\text{LSR}) \simeq +38 \text{ km s}^{-1}$ from the centroid of the emission lines. This value coincides within the errors with $\simeq +33 \text{ km s}^{-1}$ obtained by Gussie & Taylor (1990) from the [O III] emission line. Hereafter, radial velocities of internal motions in the nebula will be quoted with respect to the systemic velocity.

Fig. 2 shows position–velocity (PV) contour maps of the [S II] 6731 emission line deduced from the spectra at PAs 0° , 45° , 90° and 135° . The [S II] emission has been spatially and spectrally resolved into several bright components. The structure of the emission line is similar at PAs 0° and 135° , in which two components denoted by A1, A2 are observed. At PAs 45° and 90° four different components are observed: B1, B2, C1 and C2. B1 and B2 as well as C1 and C2 are located symmetrically with respect to the centroid of the line feature. An elliptical-shaped, faint emission, denoted by D in Fig. 2, is seen at all PAs surrounding all components; D is characterized by a steep intensity gradient on the PV maps.

Fig. 3 presents PV maps of the [N II] 6583 emission line at PAs 0° and 90° . The PV maps at PAs 45° and 135° (not shown here) are very similar to those at PAs 90° and 0° , respectively. The bright components A1, A2, B1 and B2 can also be recognized in the [N II] emission, whereas C1 and C2 are marginally detected. D appears very prominent in [N II].

In addition, faint [N II] emission, denoted by H, surrounds the other components and is extended in both spatial and spectral directions. The PV maps of the H α emission line (not shown here) are similar to those of the [N II] line (Fig. 3).

To analyse the spatiokinematical properties of Cn 3-1, we have obtained the velocity field by fitting a multiGaussian line profile on each row (spatial direction) of the two-dimensional frames at all observed PAs. Fig. 4 presents the results obtained from the [S II] emission line (Fig. 2). Line splitting is observed in the central regions ($\pm 1 \text{ arcsec}$) of the nebula. A maximum velocity difference of line splitting of $\simeq 33 \text{ km s}^{-1}$ is observed at the stellar position (defined by the position of the continuum intensity peak in the two-dimensional spectra). At other positions, the radial velocity of the [S II] emission is close to the systemic velocity, although at PAs 45° and 90° , differences of $\simeq 3\text{--}5 \text{ km s}^{-1}$ are observed between the NE–E and SW–W regions of the nebula, the SW–W regions being slightly blueshifted.

Fig. 5 shows the H α and [N II] emission-line profiles observed at the stellar position. This spectrum has been obtained by co-adding the rows around $\pm 1.1 \text{ arcsec}$ from the stellar position and averaging over the four PAs. Line splitting is not observed in the [N II] and H α emission lines, but there is a single narrow component at the systemic velocity and with a velocity width (FWHM) of $\simeq 40 \text{ km s}^{-1}$ (instrumental resolution corrected) in both the H α and [N II] emissions. The fact that the velocity widths of H α and [N II] are identical to each other suggests that different kinematical components, which have not been spectrally resolved, may be contributing to the [N II] emission line, as in the case of the [S II] line (see Figs 2 and 3). In addition, very faint extended wings are observed in the H α emission. The wings are symmetrical with respect to the systemic velocity, and a total width of $\simeq 660 \text{ km s}^{-1}$ is traced down to the continuum level. The extended H α wings suggest the presence of a broad component. Extremely faint wings seem also to be present in the [N II] emission (see below). Both broad and narrow components are also observed in [N II] and H α at distances between ± 1.1 and $\pm 4.3 \text{ arcsec}$ from the centre. The narrow component presents a similar kinematical behaviour to that observed in the [S II] emission line, at each PA. The broad component is clearly observed in [N II] (see Fig. 3) with a total velocity width of $\simeq 460 \text{ km s}^{-1}$, whereas in H α it presents similar properties to those obtained at the stellar position (see above).

Faint emission from component H can be traced in [N II] and H α up to $\simeq \pm 18 \text{ arcsec}$ from the stellar position at all PAs. The emission from H indicates a circular halo around the nebula. Recent images obtained by us (to be published elsewhere) confirm the existence of this halo. Fig. 6 shows

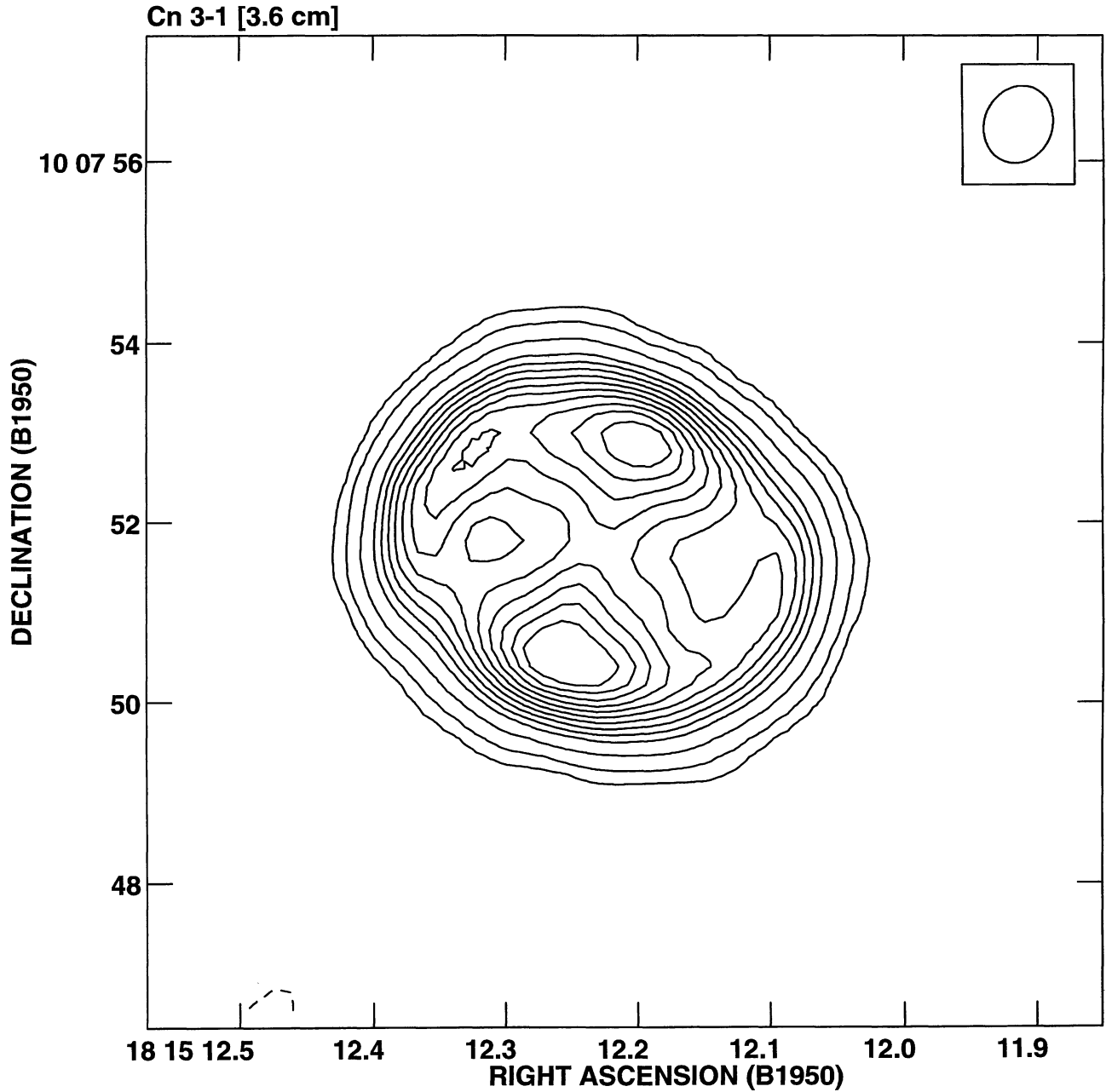


Figure 1. Contour 3.6-cm continuum map of Cn 3-1 obtained with the VLA-B. Contour levels are $-3, 6, 12, 24, 40, 50, 60, 70, 80, 90, 100, 110, 120$ and 130 times $30 \mu\text{J beam}^{-1}$, the rms noise in the map. The beamsize is indicated at the top right corner ($0.88 \times 0.75 \text{ arcsec}^2$, $\text{PA} = -23^\circ$).

the $\text{H}\alpha$ and $[\text{N II}]$ emission line profiles from the halo. This spectrum was obtained by co-adding the rows between $\approx \pm 4.3$ and $\approx \pm 18 \text{ arcsec}$ from the stellar position and averaging over all PAs. The broad and narrow components can also be recognized in the $\text{H}\alpha$ and $[\text{N II}]$ profiles of the halo. The total width of the wings can be traced up to $\approx 660 \text{ km s}^{-1}$ in $\text{H}\alpha$ and $\approx 460 \text{ km s}^{-1}$ in $[\text{N II}]$. The velocity width (FWHM) of the narrow component is $\approx 40 \text{ km s}^{-1}$ in both emission lines. The radial velocity of both components coincides with the systemic velocity. It is important to note that this result is obtained at all spatial positions and all PAs. The kinematical properties of the two emission components

in the halo are identical to those observed at other positions. The main difference is that the contribution of the broad component to the total flux in the halo is ≈ 70 per cent in $\text{H}\alpha$ and ≈ 50 per cent in $[\text{N II}]$; these values are larger than the corresponding ratios at other positions.

As already mentioned, bright components have been identified in the PV maps. In $[\text{S II}]$, at $\text{PA } 0^\circ$, A1 and A2 are separated by $\approx 2.9 \text{ arcsec}$, and their radial velocity coincides with the systemic velocity (Fig. 2). At $\text{PA } 135^\circ$, the separation between A1 and A2 is $\approx 2.7 \text{ arcsec}$, the radial velocity of A2 coincides with the systemic velocity, and A1 is blue-shifted by $\approx -2 \text{ km s}^{-1}$. At $\text{PA } 45^\circ$ and 90° , B1 and B2 are

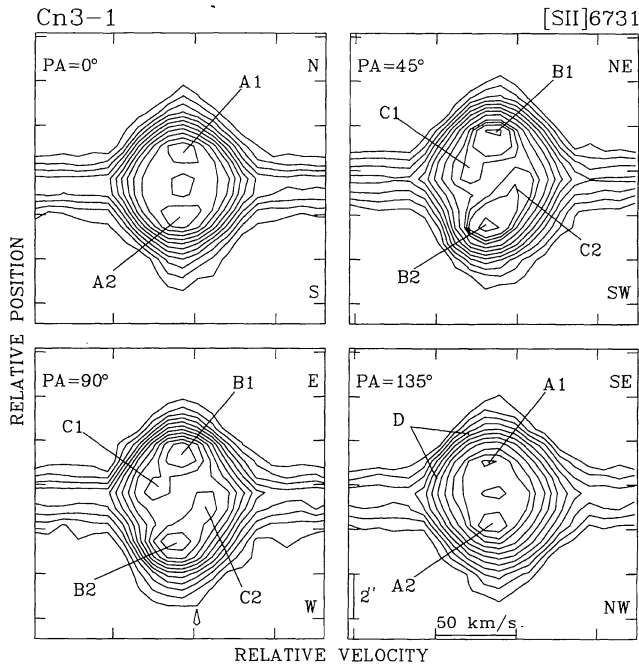


Figure 2. Position–velocity contour maps of the [S II] 6731 emission line in Cn 3-1 at PAs 0°, 45°, 90° and 135°. The contours are logarithmically separated by a factor $\sqrt{2}$ in intensity. The identified line components are denoted by A1, A2, B1, B2, C1, C2 and D.

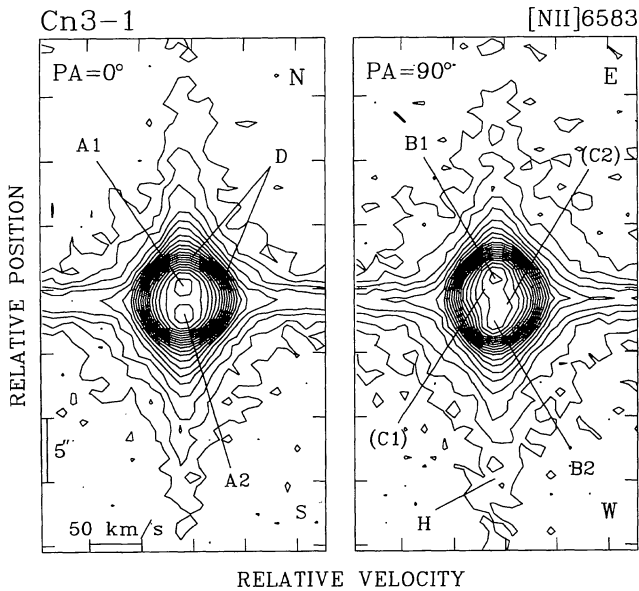


Figure 3. Position–velocity contour plots for the [N II] 6583 emission line in Cn 3-1 at PAs 0° and 90°. The contours are logarithmically separated by a factor $\sqrt{2}$ in intensity. Identified line components are indicated (see also Fig. 2).

separated by ≈ 3.9 arcsec and by ≈ 3.5 km s $^{-1}$ in radial velocity; B1 is slightly redshifted, and B2 is slightly blue-shifted. C1 and C2 are separated by ≈ 0.7 arcsec and by ≈ 28 km s $^{-1}$ in radial velocity at both PAs; C1 is blueshifted,

and C2 is redshifted. None of these components has been spatially resolved (angular size ≤ 2 arcsec). The velocity width (FWHM) is ≈ 25 km s $^{-1}$ in all components. This value is relatively small compared to the total velocity width of ≈ 95 km s $^{-1}$ obtained for the entire [S II] emission line. These results suggest that the emission from the bright components arises in geometrically thin regions of the nebula. In the PV maps of the [N II] emission line (Fig. 3), A1 and A2 are separated by ≈ 2.3 arcsec, whereas B1 and B2 are separated by ≈ 3.2 arcsec.

Component D is better observed in the [N II] emission line (Fig. 3). Its intensity gradient is steeper between ≈ 25 and ≈ 3 per cent levels of the intensity peak at all PAs. We will therefore consider it to be limited by these two intensity levels. D presents in the PV maps an elliptical shape, the angular diameter changing with PA – maximum angular diameter observed at PA 90°, minimum at PA 0° (Fig. 3). The angular diameter of the inner edge (25 per cent level) and of the outer edge (3 per cent) of D are ≈ 6.4 and ≈ 8.4 arcsec at PA 90°, respectively. The same values for PA 0° are ≈ 5.5 and ≈ 7.8 arcsec, respectively. The angular diameter at PA 45° (135°) is similar to but slightly lower (larger) than that at PA 90° (0°). Obviously, D is elongated at PA 90°, which is close to the major nebular axis observed in the radio continuum (Fig. 1). It is worth noting that the angular diameter at 25 per cent level coincides with the size of the radio continuum emission at the 3σ level, at all PAs.

Mean line intensity ratios have been obtained by integrating the emission lines along the spatial direction and then averaging over the four PAs. The mean [N II]/H α and [S II]/H α ratios are ≈ 0.83 and ≈ 0.056 , respectively. These values are substantially higher than those typically found in low-excitation PNe (e.g. Aller & Czyzak 1983). The mean [S II] 6716/6731 line intensity ratio is ≈ 0.516 . Assuming $T_e \approx 10^4$ K, we obtain $N_e \approx 8 \times 10^3$ cm $^{-3}$, comparable to other estimates and somewhat higher than the value deduced from the radio continuum (see Table 1).

In order to analyse possible variations of the line intensity ratios, relative line intensities were estimated by co-adding the rows in three spatial regions: a central region within ± 1.1 arcsec from the stellar position; a second region between ± 1.1 and ± 4.3 arcsec; and a third region between ± 4.3 and ± 18 arcsec, representative of the halo. The ratios present small differences of ≈ 2 –5 per cent among the different PAs (except for the [S II]/H α ratio, see below) and have been averaged. In the central region, [N II]/H α is ≈ 0.77 and [S II]/H α is ≈ 0.033 . The value of [N II]/H α is relatively high, whereas the value of [S II]/H α is typical for low-excitation PNe. In the second region, [N II]/H α and [S II]/H α are ≈ 0.86 and ≈ 0.078 , respectively. We note that [S II]/H α is systematically higher at PAs 45° and 90° (≈ 0.083) than at PAs 0° and 135° (≈ 0.073). Because the bright components B1 and B2 are observed in the second region at PAs 45° and 90° but not at PAs 0° and 135° (Fig. 1), we can conclude that B1 and B2 present the highest [S II]/H α ratio in the nebula. In the halo, the mean [N II]/H α is ≈ 0.46 . However, if the two kinematic components observed in the halo (Fig. 6) are considered separately, [N II]/H α is ≈ 0.86 in the narrow component and ≈ 0.37 in the broad one. The [N II]/H α ratio in the narrow component of the halo is identical to that found in the second region. No particular variation of N_e has been found.

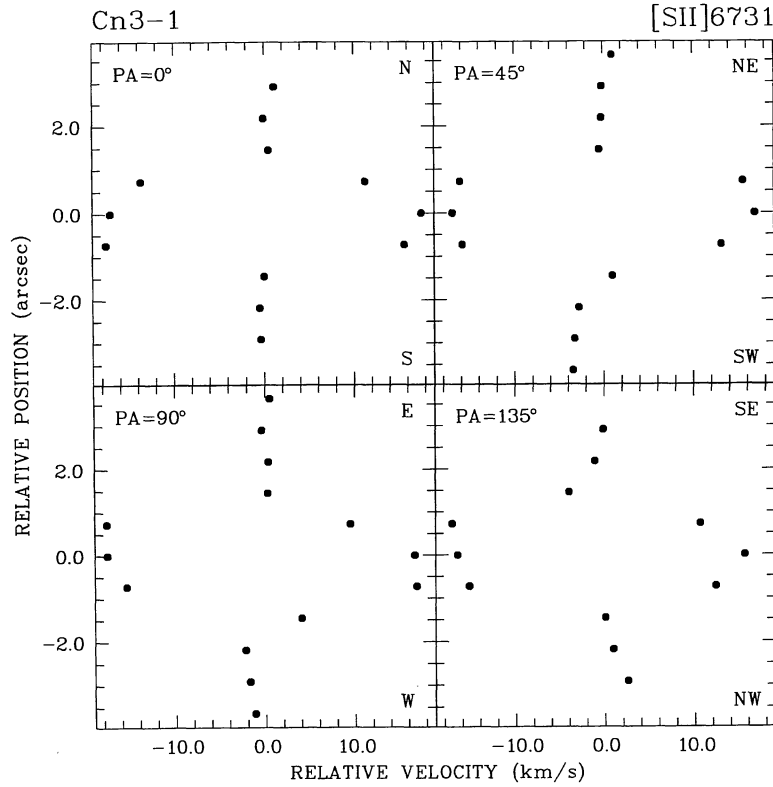


Figure 4. Position–velocity plots of the radial velocity in Cn 3-1 deduced from the [S II] 6731 emission line as observed at the different PAs. The origin (0, 0) corresponds to the systemic velocity and to the position of the central star.

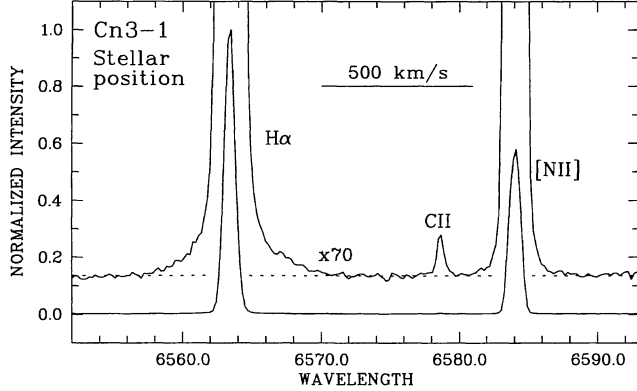


Figure 5. H α and [N II] 6583 emission-line profiles observed at the stellar position in Cn 3-1. The spectrum is presented at two different scales in order to show the extremely faint extended wings of the emission lines. The dashed line represents the stellar continuum extrapolated from the region 6650–6750 Å.

3.2 Discussion

The radio continuum image, the elliptical shape of component D in the PV maps, and the variation of the angular diameter of D with PA show that Cn 3-1 is an ellipsoidal PN. The major axis is oriented at PA $\simeq 72^\circ$ and is tilted so that the NE regions of the nebula point away from the observer, whereas the SW regions point towards the observer. Nevertheless, the radial velocity difference between the NE–E and SW–W parts of the nebula is very small, suggesting that the inclination angle is also very small. The equatorial zone

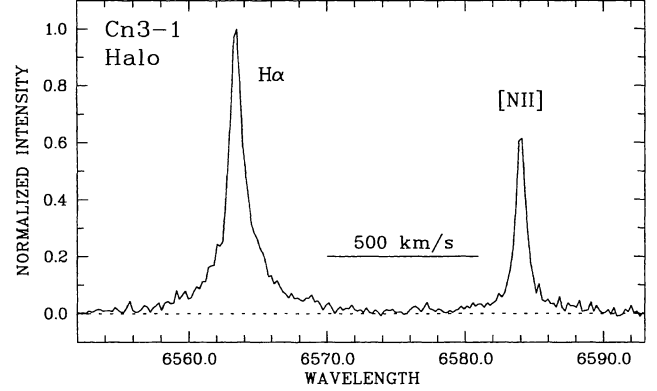


Figure 6. H α and [N II] 6583 emission-line profiles from the halo (component H) of Cn 3-1.

of the ellipsoid is particularly bright, as indicated by the presence of the strong maxima at the minor nebular axis (Fig. 1). The bright components A1 and A2 are probably related to the maxima observed in the radio continuum. C1 and C2 can also be attributed to the equatorial zone. This is indicated by the relatively high brightness of C1 and C2, the small angular separation between these components, which is expected if the equatorial zone is seen almost edge-on, and by the fact that C1 is blueshifted and C2 is redshifted in agreement with the inclination of the polar axis. B1 and B2 are probably related to the bright point symmetric arcs.

An estimate for the inclination angle of the equatorial plane can be obtained from the angular separation between

C1 and C2 (≈ 0.7 arcsec) and that between A1 and A2 at PA 0° (≈ 2.9 arcsec) which is the closest one to the minor nebular axis. Assuming that the equatorial region is circular, we obtain an inclination angle of $\approx 14^\circ$ for the equatorial plane with respect to the line of sight. The equatorial expansion velocity, related to the radial velocity separation of C1 and C2, is $\approx 14 \text{ km s}^{-1}$. The polar expansion velocity is difficult to estimate, because we do not know whether the arcs actually represent the polar regions of the ellipsoid. If we consider a projected size of ≈ 3.9 arcsec for the major axis and assume that the expansion velocity is proportional to the radius in the ellipsoid, the polar expansion velocity would be $\approx 20 \text{ km s}^{-1}$ and the axis ratio ≈ 1.4 . We note that the equatorial expansion velocity is rather low compared to typical expansion velocities of PNe. The kinematical age is ≈ 1300 yr, which is compatible with the early evolutionary stage of Cn 3-1.

The halo exhibits emission and kinematical properties which are almost identical to that observed in the central regions of Cn 3-1. In particular, the narrow nebular component and the broad component can be recognized in the emission from the halo. We note that the broad component cannot originate in the halo itself. The large velocity width suggests that this component could be related to the Wolf-Rayet type central star of Cn 3-1 (Lutz 1977), although [N II] emissions do not appear associated to Wolf-Rayet stars. On the other hand, the different velocity widths in H α and [N II] suggest scattering effects in the broad component.

All these results strongly suggest that most of the emission from the halo is reflected light. The halo probably represents the envelope remnant ejected by the AGB progenitor of Cn 3-1, which still contains large amounts of neutral material. It is probable that the Mg I absorption lines in Cn 3-1 detected by Gurzadyan et al. (1991) originate in the halo. If the halo is a reflection nebula, its expansion velocity can not be deduced from the observed velocity width (FWHM). By assuming an expansion velocity of $\approx 10 \text{ km s}^{-1}$, typical of red giant envelopes, the kinematical age of the halo is $\approx 2 \times 10^4$ yr, much larger than the kinematical age of the ellipsoid.

The radial velocity of the narrow emission from the halo coincides with the systemic velocity at all positions and at the four PAs. The extended wings are symmetrical with respect to the systemic velocity at all positions and at all PAs. These results and the reflection nature of the halo can be used to obtain information about the distribution of neutral scattering material in the halo. It is well known that an expanding anisotropic distribution of scattering material around an emission line source introduces shifts in the radial velocity of the reflected emission lines; the radial velocity shifts depend on the direction and magnitude of the velocity vector of the scattering material with respect to the observer (see Solf 1994). Let us assume that the halo around Cn 3-1 is ellipsoidal, with the major axis oriented at PA 72° and tilted by 14° with respect to the plane of the sky, similarly to the ionized ellipsoid. In this geometry, the 'mean' velocity vector at PA 72° points away from the observer, and the 'mean' velocity vector at PA 252° points towards the observer. Following Solf (1994, his equations 1a and 1b) and assuming a velocity of $\approx 10 \text{ km s}^{-1}$ for the scattering material, the observed radial velocity of the emission lines

after reflection in the halo would be $\approx +12 \text{ km s}^{-1}$ at PA 72° and $\approx +8 \text{ km s}^{-1}$ at PA 252° , with respect to the systemic velocity of Cn 3-1. In our case, no long-slit spectrum has been obtained along PA 72° , but for PAs close to the major axis, the radial velocities would be still comparable to, although probably slightly lower than, those quoted above. Radial velocities of that order should have been detected at the positions of the halo in the spectra at PAs 45° and 90° , because much lower radial velocities have been measured at other positions of the nebula (Fig. 4). This would also be true, although the velocity of the scattering material would be a factor ≈ 2 lower than that assumed above. From these results, we conclude that the distribution of neutral material in the halo is largely isotropic. This result is also indicated by the fact that the [N II]/H α ratio in the halo does not vary with the PA. Therefore the mass ejection has probably been isotropic during the last $\approx 2 \times 10^4$ yr of the AGB progenitor of Cn 3-1.

On the other hand, non-spherical shells in PNe are usually attributed to an anisotropic density distribution in the red giant envelope, which constrains the expansion in an equatorial plane (e.g. Balick 1987). However, in the case of Cn 3-1, no anisotropic density distribution can be inferred from our data. In this context it should be mentioned that the broad component is much weaker in the direction of the central star than towards the halo. This seems to indicate that more absorbing material exists in the equatorial plane of Cn 3-1 than above that plane. However, if so, one would expect that the [N II]/H α ratio and the radial velocity in the halo would present variations with PA, which are not observed. A satisfactory explanation for the intensity variation of the broad component has not been found.

We have considered above Cn 3-1 without taking into account the bright point-symmetric arcs (B1 and B2). The arcs do not fit in a simple ellipsoidal model. Our results suggest that the arcs are relatively collimated filaments which seem to be located within the ellipsoid. They are not symmetrical with respect to the major nebular axis. The observed point-symmetry both in space and in velocities is difficult to interpret as a result of projection effects or instabilities in the shell. The point-symmetric arcs in Cn 3-1 resemble other point-symmetric structures observed in PNe. In particular, we find similarities between Cn 3-1 and NGC 6543. Both PNe present an ellipsoidal shell with a bright equatorial ring-like zone and bright point-symmetric filaments located within the shell (Miranda & Solf 1992). The properties of the arcs in Cn 3-1 resemble those found in components DD' in NGC 6543. The arcs and DD' appear as oblique filaments in the ellipsoid, which are not related to the major nebular axis. The [N II]/H α and [S II]/H α ratios in the arcs are very similar to those in DD', and suggest shock excitation and an overabundance of N (see also Balick et al. 1994). Point-symmetric collimated structures in PNe have been attributed to some sort of collimated ejections along a precessing or rotating axis (see references above). If the arcs in Cn 3-1 are related to this mechanism, then the orientation of the ejection axis must have been very different from that of the polar nebular axis, and the formation of the arcs must have occurred in a very short time compared to the age of the ellipsoid, as suggested by Miranda & Solf (1992) for the formation of the various point-symmetric collimated components in NGC 6543.

4 M3-27

4.1 Results

A compact unresolved radio continuum source (≤ 0.6 arcsec) is detected in this PN with a flux density of 0.9 mJy at 3.6 cm. From these values, assuming $T_e \simeq 10^4$ K, we estimate $N_e \simeq 9 \times 10^3$ cm $^{-3}$, $EM \simeq 10^6$ pc cm $^{-6}$, and $M(\text{H II}) \simeq 3 \times 10^{-4} M_\odot$.

Fig. 7 presents PV contour maps of the [S II] 6731 and [N II] 6583 emission lines as observed at PAs 0° and 90°. Although both emission lines appear rather compact along the spatial direction in the PV maps, some structure can be recognized in the emission features. At PA 90°, the [S II] emission line appears tilted with respect to the stellar continuum. The eastern part of the [S II] line is blueshifted, and the western part is redshifted. The observed radial velocity difference along the line feature is $\simeq 8$ km s $^{-1}$. At PA 0°, no velocity gradient is observed. A similar result is found in the [N II] emission. The emission features have not been spatially resolved (FWHM ≤ 1.4 arcsec). The velocity width (FWHM) is $\simeq 33$ km s $^{-1}$ in both [N II] and [S II] lines. The systemic velocity (LSR) is $\simeq -24$ km s $^{-1}$, comparable to the value deduced by Tamura, Kazes & Shibata (1990).

Fig. 8 presents the spectrum of M3-27 integrated along the spatial direction obtained from the spectrum at PA 0°. H α exhibits a type III P Cygni profile consisting of two emission peaks at $V(\text{LSR}) \simeq -84$ and -7 km s $^{-1}$, separated by an absorption reversal at $V(\text{LSR}) \simeq -55$ km s $^{-1}$. From the centroid of the H α emission feature we obtain a radial velocity (LSR) of $\simeq -28$ km s $^{-1}$, compatible with the value deduced from the forbidden lines. Very extended wings are observed in the H α emission. The red wing can be traced up to $\simeq 1500$ km s $^{-1}$ before reaching the continuum, from the velocity centroid of the line; the blue wing extends beyond the observed spectral range. If we assume symmetry with respect to the velocity centroid, the total velocity width of H α is $\simeq 3000$ km s $^{-1}$.

Fig. 9 shows a PV contour map of the H α emission as observed at PA 90°. An identical structure is observed at PA 0° (not shown here). The PV map of H α is completely different from those of [S II] and [N II] (Fig. 7). Faint H α emission can be traced up to $\simeq \pm 12$ arcsec from the stellar position at both PAs 0° and 90°. Remarkably, the type III P Cygni profile and extended wings can be recognized at each spatial position along the slit. The radial velocities of the emission and absorption components coincide at all spatial positions and at PAs 0° and 90° with those quoted above.

The [S II]/[N II] ratio of $\simeq 0.16$ deduced from our spectra is different from the value of $\simeq 0.07$ obtained by Barker (1978). The [S II] 6716/6731 ratio of $\simeq 0.557$ indicates $N_e \simeq 5 \times 10^3$ cm $^{-3}$, comparable to other estimates. This value, though, is lower than that deduced from the radio continuum emission (Table 1) and from the [O III] emission lines (Feibelman 1985). This may be due to stratification within the nebula and/or to quenching of the [S II] lines in the high-density limit.

4.2 Discussion

As it has been shown above, the PV maps of the [S II] and [N II] emission lines present differences with PA, suggesting

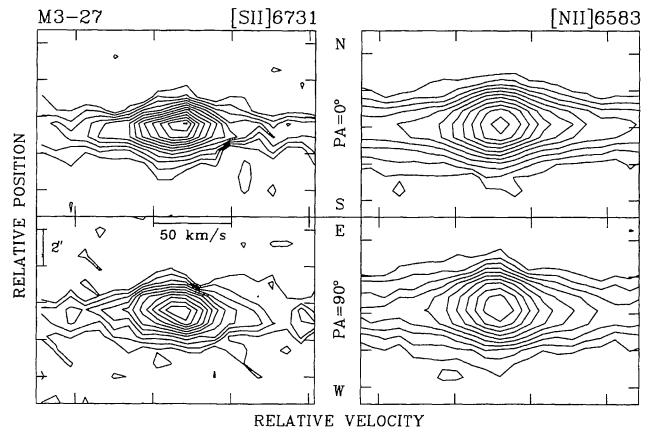


Figure 7. Position–velocity contour maps of the [S II] 6731 and [N II] 6583 from M3-27 at PAs 0° and 90°. The contours are logarithmically separated by a factor $2^{1/2}$ ([S II]) and $2^{1/2}$ ([N II]) in intensity.

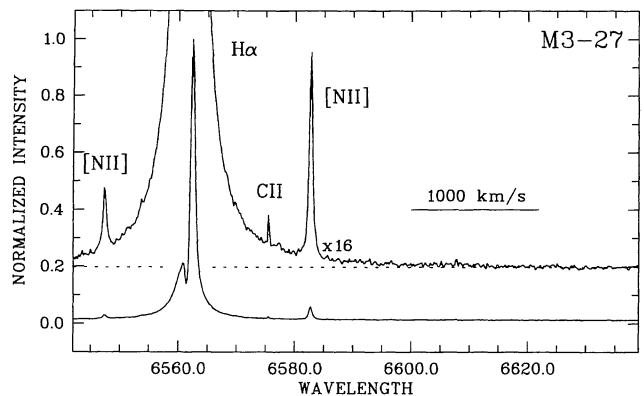


Figure 8. Spectrum of M3-27 in the range 6540–6590 Å. The spectrum is presented at two different intensity scales in order to show the extended wings of the H α emission. Extrapolated stellar continuum from the 6650–6750 Å region is plotted as a dashed line.

that the inner nebular regions in which these emission lines arise are not spherically symmetric. The tilt of the [S II] and [N II] emission features on the PV maps suggests that the inner region is elongated along an axis which lies closer to PA 90° than at PA 0° where no tilt is observed. Details of the inner region cannot be obtained from our data. Nevertheless, it is worth noting that the PV maps of the [N II] and [S II] lines in M3-27 are similar to those observed in the compact very young PN VY 2-2 and are compatible with a bipolar flow (see Miranda & Solf 1991). The expansion velocity of the inner regions, deduced from the velocity width (FWHM) of the [N II] and [S II] emissions, is $\simeq 17$ km s $^{-1}$. By combining the expansion velocity and the optical radius of ≤ 0.7 arcsec, we obtain a kinematical age of ≤ 530 yr.

The H α emission must arise in regions different from the compact inner region in which the [S II] and [N II] emission arises. None of the H α components coincides in radial velocity with the systemic velocity obtained from the forbidden lines, excluding the possibility that the H α components are related to the inner shell. The most probable explanation

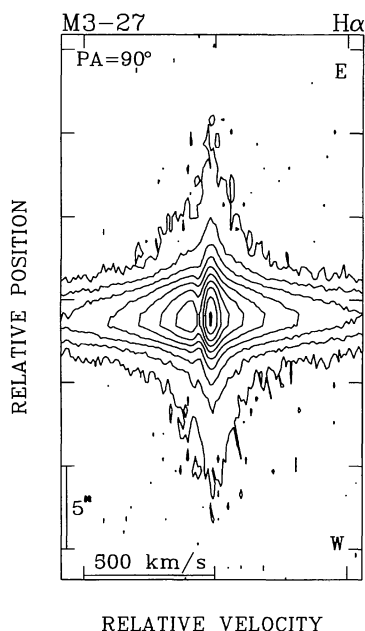


Figure 9. Position–velocity map of the H α emission from M 3-27 at PA 90°. The contours are logarithmically separated by a factor 2 in intensity.

for the origin of the P Cygni profile is that it originates in an ionized wind from the central star. In this context, the absorption reversal represents self-absorption in the wind (see Adams 1975). It is interesting to note that the H α profile of M 3-27 presented by Tamura et al. (1990) exhibits a single symmetric peak and probably extended wings, but not a second peak and an absorption reversal as in ours (Fig. 8). Although the spectral resolution in the spectrum by Tamura et al. (1990) is lower than ours, these data suggest variability of the H α emission. If the H α emission is variable, the contribution of the H α wings at the position of the [N II] lines may be variable, too. Therefore variations of the [S II]/[N II] ratio might also be due to H α variability.

The extended H α emission can be attributed to a halo. The halo can be identified with the remnant envelope of the AGB progenitor of M 3-27. Because the H α profile from the halo is identical to the stellar H α profile, the observed emission probably is reflected in neutral material in the halo. As in the case of Cn 3-1, reflection in the halo does not introduce shifts in the radial velocity of the emission lines. This suggests that the distribution of neutral material in the halo may be isotropic. By assuming an expansion velocity of ≈ 10 km s $^{-1}$ (see above), the kinematical age of the halo if $\approx 1.7 \times 10^4$ yr, much higher than the value deduced for the inner region observed in the forbidden lines.

From these results, we identify the inner compact region detected in the forbidden lines with the ionized shell of M 3-27. The kinematical age and ionized mass estimated for this region indicate that M 3-27 is a very young PN. The inner shell has not been detected in the H α emission because this emission is dominated by strong stellar emission. It is interesting to note that type III P Cygni profiles and/or very extended wings in the H α emission are commonly observed in very young PNe and protoPNe such as M 2-9 (Balick 1989), IC 4997 (Feibelman, Aller & Hyung 1992; Miranda

et al. 1996), Mz 3 (López & Meaburn 1983) and M 1-92 (Solf 1994).

5 CONCLUSIONS

We have carried out long-slit optical spectroscopy and VLA-B radio continuum ($\lambda = 3.6$ cm) observations of the compact PNe Cn 3-1 and M 3-27. Our main conclusions can be summarized as follows.

(1) Cn 3-1 is an ellipsoidal PN with a low equatorial expansion velocity of ≈ 14 km s $^{-1}$. A bright, ring-like zone seen almost edge-on characterizes the equator of the ellipsoid. Two point-symmetric arcs have been detected in the nebula. The arcs appear as filamentary structures. Their origin could be related to collimated bipolar ejections along a rotating axis. The deduced kinematical age (≈ 1300 yr) and ionized mass ($\approx 4 \times 10^{-2} M_{\odot}$) are compatible with Cn 3-1 being a young PN.

(2) Relatively high [N II]/H α and [S II]/H α line intensity ratios (≈ 0.83 and ≈ 0.056) are found in Cn 3-1. Maximum values of the [S II]/H α ratio ≈ 0.083 are found in the arcs, suggesting a possible contribution from collisional excitation.

(3) The [N II] and [S II] emission lines detected in M 3-27 arise in a compact (≤ 1.4 arcsec), probably non-spherical region, which we identify with the ionized shell of the nebula. The kinematical age (≤ 530 yr) and ionized mass ($\approx 3 \times 10^{-4} M_{\odot}$) estimated for this shell indicate that M 3-27 is a very young PN.

(4) The H α emission from M 3-27 is dominated by stellar emission. H α presents a type III P Cygni profile with very extended wings (≈ 3000 km s $^{-1}$). Variability of the H α profile is suggested by comparing our results with other data previously published.

(5) Extended haloes have been spectroscopically detected in both PNe with angular diameters of ≈ 36 arcsec in Cn 3-1 (H α and [N II] emissions) and ≈ 24 arcsec in M 3-27 (H α emission). The haloes very probably represent material ejected during the AGB phase of the progenitors of both PNe. An analysis of the kinematical and emission properties of the haloes strongly suggests that they are reflection nebulosities and still contain much neutral material, and that the distribution of neutral material in them is isotropic.

ACKNOWLEDGMENTS

JMT and RV are supported in part by DGICYT grant PB95-0066 and by Junta de Andalucía (Spain). LFM and CE are supported partially by DGICYT grant PB94-165 (Spain). JAL acknowledges continuous support from CONACYT and DGAPA-UNAM. RV thanks Instituto de Cooperación Iberoamericana (Spain) for his graduate scholarship, and DGAPA-UNAM (México) for complementary support. LFM is grateful to O. Alonso and N. Cardiel for fruitful discussions during the interpretation of the data.

REFERENCES

Acker A. et al., 1992, Strasbourg–ESO Catalogue of Galactic Planetary Nebulae. European Southern Observatory, Garching

- Adams T. F., 1975, *ApJ*, 202, 114
 Ahern F. J., 1978, *ApJ*, 223, 901
 Aller L. H., Czyzak S. J., 1983, *ApJS*, 51, 216
 Balick B., 1987, *AJ*, 94, 671
 Balick B., 1989, *AJ*, 97, 476
 Balick B., Perinotto M., Maccini A., Terzian Y., Hajian A., 1994, *ApJ*, 424, 800
 Barker T., 1978, *ApJ*, 219, 914
 Cahn J. H., Kaler J. B., Stanghellini L., 1992, *A&AS*, 94, 399
 Corradi R. L. M., Manso R., Mampaso A., Schwarz H. E., 1996, *A&A*, 313, 913
 Feibelman W. A., 1995, *PASP*, 97, 404
 Feibelman W. A., Aller L. H., Hyung S., 1992, *PASP*, 104, 339
 Gieseeking F., Becker I., Solf J., 1985, *ApJ*, 295, L17
 Gurzadyan G. A., Egikyan A. G., Terzian Y., 1991, *Ap&SS*, 176, 9
 Gussie G. T., Taylor A. R., 1990, *PASP*, 102, 232
 Hora J. L., Latter W. B., 1996, *ApJ*, 461, 288
 Kingsburgh R. L., English J., 1992, *MNRAS*, 259, 635
 López J. A., Meaburn J., 1983, *MNRAS*, 204, 203
 López J. A., Meaburn J., Palmer J., 1993, *ApJ*, 415, L135
 Luhman K. L., Rieke G. H., 1996, *ApJ*, 461, 298
 Lutz J. H., 1977, *ApJ*, 211, 469
 Mezger P. G., Henderson A. P., 1967, *ApJ*, 147, 490
 Miranda L. F., 1995, *A&A*, 304, 531
 Miranda L. F., Solf J., 1991, *A&A*, 252, 331
 Miranda L. F., Solf J., 1992, *A&A*, 260, 397
 Miranda L. F., Torrelles J. M., Eiroa C., 1995, *ApJ*, 446, L39
 Miranda L. F., Torrelles J. M., Eiroa C., 1996, *ApJ*, 461, L111
 Sabbadin F., 1984, *MNRAS*, 209, 889
 Sabbadin F., Bianchini A., Hamzaoglu E., 1983, *A&AS*, 52, 395
 Schwarz H. E., Corradi R. L. M., Melnick J., 1992, *A&AS*, 96, 23
 Solf J., 1994, *A&A*, 282, 567
 Tamura S., Kazes I., Shibata K. M., 1990, *A&A*, 237, 479